

Three-dimensional variable-angle nuclear magnetic resonance exchange spectroscopy without rotor axis hopping

Y. K. Lee,^{a)} L. Emsley,^{b)} R. G. Larsen, K. Schmidt-Rohr, M. Hong, L. Frydman,^{c)}
G. C. Chingas, and A. Pines^{d)}

Materials Sciences Division, Lawrence Berkeley Laboratory, and Department of Chemistry, University of California, Berkeley, California 94720

(Received 15 February 1994; accepted 22 April 1994)

Slow, large-amplitude chain motions play an important role in determining the macroscopic mechanical properties of polymers. Although such motions have been studied quantitatively by two-dimensional (2D) nuclear magnetic resonance (NMR) exchange experiments, overlapping anisotropic patterns hamper spectral analysis, and limit applications. Variable angle correlation spectroscopy (VACSy) has proven useful in resolving such problems for rapidly spinning samples by separating anisotropic spectral patterns according to isotropic chemical shifts. In a previous study [J. Am. Chem. Soc. **115**, 4825 (1993)], we described a three-dimensional (3D) NMR experiment that incorporates the VACSy method and a hop of the rotor axis to correlate the isotropic chemical shifts to 2D anisotropic exchange patterns. The hop of the rotor axis, however, presents experimental difficulties and limits the range of motional rates that may be studied. We present in this paper a new 3D VACSy exchange experiment that obtains the same correlations without the need for the rotor axis hop. A series of 2D exchange spectra are recorded with the sample spinning at different rotation axis angles. Then using the scaling of the anisotropic frequency at the different angles, we construct the data onto a 3D matrix so that a Fourier transformation directly yields the desired correlations. The technique is applied to ¹³C exchange NMR to study the slow molecular motion of ordered isotactic polypropylene.

I. INTRODUCTION

Much of the success of nuclear magnetic resonance (NMR) experiments relies on the ability to resolve resonant frequencies for each chemical site. The high resolution provided by technical advances in high-field superconducting magnets and the development of multidimensional techniques has made possible NMR studies of increasingly complex biological molecules in solution.¹ High resolution NMR in solids has similarly led to studies of more complex systems. However, unlike liquid-state NMR, where the fast tumbling motion of molecules provides a high resolution spectrum naturally, solid-state NMR requires experimental averaging techniques to remove the broad orientation-dependent components of the spectrum.^{2,3} The removal of these anisotropic components, however, has the unfortunate consequence of also removing structural and dynamical information, which makes the ability to selectively reintroduce anisotropic spectral information an important aspect of solid-state NMR. Experiments may be designed to yield both the high resolution needed to study complex systems and the anisotropic information needed to characterize the structural and dynamical properties of molecules. Useful techniques of this type include 2D and 3D experiments, where high reso-

lution, isotropic frequencies along one dimension are correlated with broad, anisotropic frequency distributions in the other dimensions.⁴⁻¹⁰

The study of polymers is one area where correlation of isotropic and anisotropic information is especially valuable. Microscopic ordering and dynamics of polymers influence important macroscopic properties such as the mechanical moduli. For example, in many polymers, the α relaxation process is directly related to slow, large-scale motions of polymer chains, while the lower temperature β relaxation process is associated with more localized dynamics, such as phenylene ring flips or side group motions.¹¹⁻¹³ Such motions may be studied by solid-state NMR in one of three motional time regimes. First, in the "fast" regime, where the correlation time τ_c is of the order of the Larmor frequency, measurements of the spin-lattice relaxation times are useful for determining motional rates. Second, in the "intermediate" regime, where τ_c is of the order of the inverse width of the anisotropic frequency distribution $\tau_c \sim 1/\Delta\omega^a$, the spectral line shapes become altered; in favorable cases, motional information may be extracted by computer-simulated fits to the anisotropic patterns.¹⁴ Finally, in the "slow" regime, where $\tau_c \gg 1/\Delta\omega^a$, a 2D exchange experiment can be used to correlate the molecular orientations at two different times, separated by a long mixing period to allow for molecular motion. The resulting 2D exchange spectrum directly reflects the probability distribution function for molecular reorientation.¹⁵ To date, most of the progress in studying molecular dynamics in the intermediate and slow regimes by NMR has been made by examining the anisotropies in either the quadrupole spectrum of ²H (Refs. 16-18) or the chemical shift spectrum of ¹³C.¹⁹⁻²¹ While these studies are poten-

^{a)}Chemical Biodynamics Division, Lawrence Berkeley Laboratory, and Graduate Group in Biophysics, University of California, Berkeley, CA 94720.

^{b)}Present address: Centre d'Études Nucléaires de Grenoble, 38054 Grenoble, France.

^{c)}Present address: Department of Chemistry (M/C 111), University of Illinois, Chicago, IL 60680-4348.

^{d)}To whom correspondence should be addressed at the University of California.

tially very powerful, they are limited in that ^2H NMR requires isotopic labeling and natural abundance ^{13}C NMR is rendered impractical in all but the simplest systems due to overlapping patterns from chemically distinct but unresolved sites.

Recently a new experiment, variable angle correlation spectroscopy (VACSYS), was introduced to correlate the isotropic and anisotropic chemical shift interactions in rotating solids.^{9,22} The basic principle of this technique is that the change in the sample rotation axis with respect to the static magnetic field \mathbf{B}_0 scales the anisotropic frequencies while leaving the isotropic frequencies invariant. Suitable processing of data acquired at different rotation axis angles provides a 2D spectrum where anisotropic patterns are separated according to the isotropic frequencies. VACSYS has been used to extract the principal chemical shift tensor values from multisite organic molecules⁹ and glasses,²³ and to study molecular dynamics in the intermediate regime.²⁴ The technique has been extended to a 3D experiment, suitable for probing dynamics in the slow regime by correlating 2D exchange patterns with a third, high resolution dimension.²⁵ One disadvantage of this 3D VACSYS exchange experiment is the need for a special apparatus to quickly change the rotor axis between arbitrary angles during the mixing delay. This creates experimental difficulties, such as mechanical strain of the electronic leads in the coil circuit, and restricts examination of short mixing delays, since the minimum time required for the rotor hop is about 30 ms.

We present in this paper an experimental simplification of the 3D VACSYS exchange technique where the need for a sudden rotor axis reorientation is removed altogether. Now the full range of motional rates in the slow regime (1 Hz–1 kHz) may be studied, limited only by T_1 relaxation and intermediate motion effects. This experiment requires the data from a series of 2D ^{13}C NMR exchange experiments, each recorded at different rotation axis orientations, to be rearranged in a 3D matrix and Fourier transformed to obtain the high resolution exchange spectrum. Section II reviews the principles of the VACSYS technique and shows how the previously developed ideas lead to our current experiment. Section III describes mathematical details involved in the data processing. Section IV describes the experimental setup and parameters used in collecting the data. Finally, Sec. V presents the analysis of the exchange spectra and comparisons with computer simulations.

II. VACSYS—GENERAL THEORY

A. Generalization of Fourier transformations and data acquisition in VACSYS

Multidimensional NMR experiments usually acquire data by incrementing the signal orthogonally along each Fourier time dimension.²⁶ For an n -dimensional experiment, there are n time periods, t_1, t_2, \dots, t_n , during which the transverse magnetization evolves. The signal is recorded by acquiring a free induction decay (FID) during t_n , following phase encoding during the previous $n-1$ time periods. By incrementing all of the time variables independently in discrete steps, the acquired signal may be represented as²⁷

$$S(t_1, t_2, \dots, t_n) = \int_{-\infty}^{\infty} I(\omega_1, \omega_2, \dots, \omega_n) \exp[i(\omega_1 t_1 + \omega_2 t_2 + \dots + \omega_n t_n)] d\omega_1 d\omega_2 \dots d\omega_n. \quad (1)$$

If fixed steps are used along each temporal dimension, the signal $S(t_1, t_2, \dots, t_n)$ can be placed on evenly spaced Cartesian grid points in an n -dimensional matrix, and a fast Fourier transform (FFT) routine may be used to obtain the spectrum $I(\omega_1, \omega_2, \dots, \omega_n)$. This method of using time increments and Cartesian data acquisition has been extended and generalized in NMR imaging. For example, it is often advantageous in NMR imaging to evolve the Fourier phase by incrementing the magnitude of the magnetic field gradient rather than time.²⁸ There are also several NMR imaging methods that take advantage of non-Cartesian data acquisition, where experimental data points no longer fall on a rectangular grid, but where gradients are manipulated so that the signal forms radial,^{29,30} skewed,³¹ or even spiral³² trajectories in the signal Fourier space. Non-Cartesian sampling of the Fourier space, however, usually requires subsequent interpolation in order to use the FFT or to display the image.

Therefore, while the usual methods of incrementing time and acquiring data orthogonally along each Fourier dimension are often experimentally convenient and facilitate the use of the FFT, *they are not fundamental requirements for multidimensional NMR experiments*. The important requirement is that the phase which the system acquires during the experiment must be separable into individual terms, each expressible as a product of two variables³³

$$\Phi = \sum_{i=1}^n \Phi_i = \sum_{i=1}^n \omega_i \tau_i, \quad (2)$$

The frequency variables ω_i define the coordinate axes for the spectral intensity distribution, and the "generalized time" variables τ_i have the units of time and define the coordinates for the signal acquisition Fourier space. These latter variables are under experimental control and are varied during the signal evolution and detection periods. Since the signal for an n -dimensional experiment is now redefined as

$$S(\tau_1, \tau_2, \dots, \tau_n) = \int_{-\infty}^{\infty} I(\omega_1, \omega_2, \dots, \omega_n) e^{i\Phi} d\omega_1 d\omega_2 \dots d\omega_n, \quad (3)$$

by integrating over the variables τ_i , the spectrum $I(\omega_1, \omega_2, \dots, \omega_n)$ can be obtained through a Fourier transformation. This generalization of time variables and signal acquisition phase space can become a powerful tool, allowing the use of new experimental parameters and procedures to extract precisely the information desired in the spectrum. The coordinates in ω space determine the variables to be correlated in the spectrum, while the coordinates in τ space specify how the FIDs should be placed in the signal acquisition phase space. An n -dimensional experiment still requires n experimental parameters that must be incremented independently to allow the signal phase space to be densely filled with data, but there is considerably more latitude in how they are chosen.

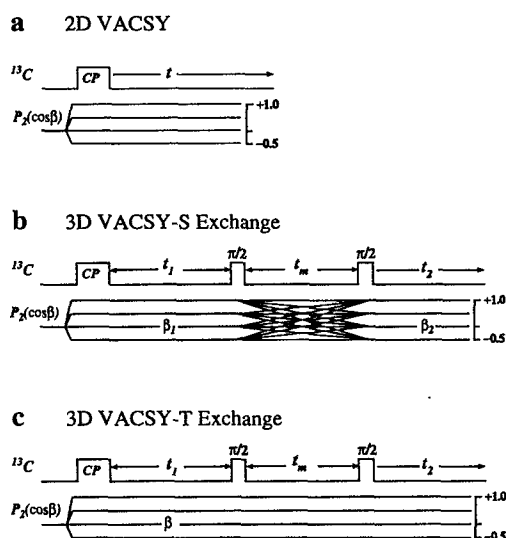


FIG. 1. Pulse sequences for three different VACSYS experiments. Below each pulse sequence is a graph of how $P_2(\cos \beta)$ is varied during the experiment. In all three experiments, a cross polarization (CP) sequence (Ref. 36) is used to create the ^{13}C magnetization, and ^1H decoupling is applied for the duration of the experiment, except during the t_m mixing delays. (a) A 2D VACSYS experiment used to correlate isotropic frequencies with 1D anisotropic spectral patterns. FIDs are acquired at different P_2 values. (b) A 3D VACSYS-S exchange experiment used to correlate the isotropic frequencies with the anisotropic frequency distributions measured before and after the t_m mixing delay. The ^{13}C magnetization evolves during t_1 with the sample spinning at the angle β_1 . One component of the magnetization is then stored for the duration of t_m , and the angle is switched to β_2 , where the FID is acquired during t_2 . Angles β_1 and β_2 are varied independently during the experiment. (c) A 3D VACSYS-T exchange experiment that obtains the same correlations as VACSYS-S, but without the need for rapid sample reorientation. A 2D exchange experiments are performed at a series of different P_2 values.

In the VACSYS experiments, the angle of the spinning axis with respect to \mathbf{B}_0 is one of the variables that controls the phase that the signal acquires. The pulse sequences and the angle profiles for three different VACSYS experiments are shown in Fig. 1; the Fourier variables and phases relevant to each experiment are listed in Table I. The design of all three experiments follows the same procedure. First, the frequency variables must be chosen to provide the desired correlation of information from the multidimensional spectrum. For the

VACSYS experiments, the isotropic frequencies in one dimension (ω_i) are correlated with anisotropic frequency distributions in the other dimensions (ω_1^a, ω_2^a), as shown in column 4 of Table I. Next, the phase acquired by the spin system during the time evolution periods is partitioned along different dimensions (column 2) such that the phase for each dimension may be factored into the desired frequency variables ω_i and the generalized time variables τ_i (column 5). Each τ_i must be distinguished from the others through different combinations of independently adjustable parameters (column 3) to ensure that the signal spans a significant portion of the multidimensional Fourier space. Finally, the FIDs are placed in τ space according to coordinates that are linear functions of time, so that the FIDs form linear trajectories whose orientations in τ space are determined by the rotation axis parameters. The data points are then interpolated onto a Cartesian grid and Fourier transformed.

B. 2D VACSYS

Figure 1(a) shows the pulse sequence for the original application of the VACSYS technique where the isotropic and anisotropic chemical shifts are correlated in a 2D experiment.⁹ The phase acquired by a crystallite in a rapidly spinning rotor, evolving under its chemical shift frequency, may be written as³

$$\Phi = \omega^i t + P_2(\cos \beta) \omega^a(\theta, \phi) t, \quad (4)$$

where ω^i is the isotropic chemical shift, $P_2(\cos \beta)$ is the second order Legendre polynomial, β is the angle of the rotation axis with respect to \mathbf{B}_0 , and $\omega^a(\theta, \phi)$ is the anisotropic chemical shift as a function of θ and ϕ the Euler angles rotating the chemical shift tensor from its principle axis frame to the rotor frame. The total phase, partitioned along two dimensions, is shown in Table I. Isotropic and anisotropic chemical shift frequencies can be correlated by allowing the signal to fill a 2D Fourier space defined by the coordinate axes $[P_2(\cos \beta)t, t]$. Each variable angle spinning FID forms a trajectory in this 2D phase space at an angle given by

$$\alpha = \tan^{-1}[R P_2(\cos \beta)] \quad (5)$$

with respect to the isotropic time axis, as illustrated in Fig. 2. Here, $R = s\omega^a/s\omega^i$, where $s\omega^a$ is the spectral width in the

TABLE I. The partitioned Fourier phases and conjugate Fourier variables for the three VACSYS experiments shown in Fig. 1.

Experiment	Components of signal phase $\Phi = \omega \cdot \tau$	Adjustable parameters	Correlated frequencies	Data coordinates in τ space
2D VACSYS	$\Phi_1 = \omega^a P_2(\cos \beta) t$ $\Phi_2 = \omega^i t$	β, t	$\begin{pmatrix} \omega_1 \\ \omega_2 \end{pmatrix} = \begin{pmatrix} \omega^a \\ \omega^i \end{pmatrix}$	$\begin{pmatrix} \tau_1 \\ \tau_2 \end{pmatrix} = \begin{pmatrix} P_2(\cos \beta) t \\ t \end{pmatrix}$
3D VACSYS-S exchange	$\Phi_1 = \omega_1^a P_2(\cos \beta_1) t_1$ $\Phi_2 = \omega_2^a P_2(\cos \beta_2) t_2$ $\Phi_3 = \omega^i t_2$	β_1, β_2, t_2	$\begin{pmatrix} \omega_1 \\ \omega_2 \\ \omega_3 \end{pmatrix} = \begin{pmatrix} \omega_1^a \\ \omega_2^a \\ \omega^i \end{pmatrix}$	$\begin{pmatrix} \tau_1 \\ \tau_2 \\ \tau_3 \end{pmatrix} = \begin{pmatrix} P_2(\cos \beta_1) t_1 \\ P_2(\cos \beta_2) t_2 \\ t_2 \end{pmatrix}$
3D VACSYS-T exchange	$\Phi_1 = \omega_1^a P_2(\cos \beta) p t_1$ $\Phi_2 = \omega_2^a P_2(\cos \beta) t_2$ $\Phi_3 = \omega^i (p t_1 + t_2)$	β, t_1, t_2	$\begin{pmatrix} \omega_1 \\ \omega_2 \\ \omega_3 \end{pmatrix} = \begin{pmatrix} \omega_1^a \\ \omega_2^a \\ \omega^i \end{pmatrix}$	$\begin{pmatrix} \tau_1 \\ \tau_2 \\ \tau_3 \end{pmatrix} = \begin{pmatrix} P_2(\cos \beta) p t_1 \\ P_2(\cos \beta) t_2 \\ p t_1 + t_2 \end{pmatrix}$

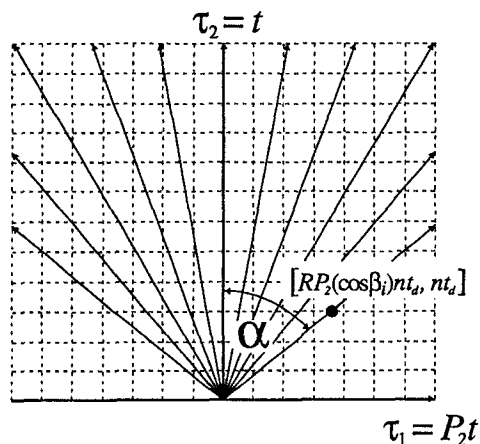


FIG. 2. Mapping of each FID in a 2D VACSy experiment. The solid rays represent the FIDs being placed on a Cartesian grid. A FID acquired at a rotation axis angle β_i is placed in the phase space as a ray inclined at an angle $\alpha = \tan^{-1}[RP_2(\cos \beta_i)]$ with respect to the isotropic axis. The coordinate shown is labeled for a data point acquired at an angle β_i with a total time evolution of nt_d .

anisotropic ω^a dimension, and sw^i is the spectral width in the isotropic ω^i dimension.⁹ Each data point acquired at a specified angle β_i has τ space coordinates

$$\tau_1 = RP_2(\cos \beta_i)nt_d, \quad \tau_2 = nt_d, \quad (6)$$

where t_d is the discrete time increment (dwell time) of the data points in each FID, and n specifies the number of time increments. Once the data points have been placed, interpolation onto the rectangular grid followed by a Fourier transformation yields the desired spectrum.

C. The 3D switched-angle VACSy (VACSy-S) exchange experiment

The pulse sequences in Figs. 1(b) and 1(c) use the VACSy technique to study slow molecular motion. The experiments are three dimensional and correlate the isotropic chemical shifts in one dimension with the anisotropic chemical shifts in the other two dimensions.²⁵ The basis of the 3D VACSy exchange experiments is the three-pulse sequence (Fig. 3) that has been used extensively in 2D exchange experiments to study molecular motion.²¹ After the initial excitation, the magnetization evolves with the chemical shift frequency

$$\omega_1 = \omega^i + \omega_1^a(\theta_1, \phi_1) \quad (7)$$

during t_1 evolution. The second pulse stores one component of the magnetization parallel to \mathbf{B}_0 for the duration of the mixing period, t_m , and the third pulse returns the magnetization to the transverse plane for detection during t_2 . If molecular reorientation occurs during t_m , the frequency during detection changes to

$$\omega_2 = \omega^i + \omega_2^a(\theta_2, \phi_2), \quad (8)$$

assuming simple reorientation which leaves the isotropic frequency unaffected. The change in the anisotropic frequency

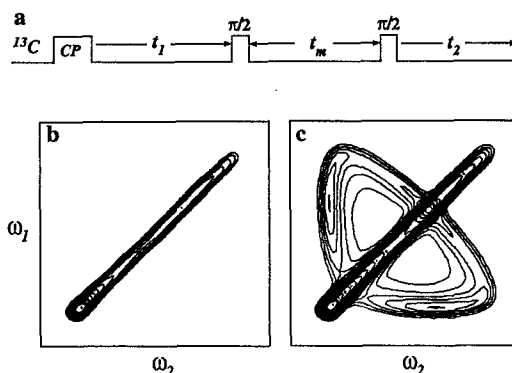


FIG. 3. The pulse sequence for the 2D exchange experiment used to study slow molecular reorientation. (a) The ^{13}C magnetization is created through cross polarization and evolves during t_1 . The second pulse stores one component of the magnetization and the third pulse returns it to the transverse plane for signal detection after the t_m delay. (b) If no molecular reorientation occurs during t_m , the 2D spectrum shows only a diagonal ridge. (c) If molecular reorientation has occurred, the 2D spectrum reveals off-diagonal patterns characteristic of the molecular motion.

results in distinctive off-diagonal patterns in the 2D spectrum [Fig. 3(c)], reflecting the type of molecular reorientation occurring during t_m .

The goal of the 3D VACSy exchange experiments is to obtain these 2D anisotropic patterns for each chemical site, requiring spectral variables defined as $[\omega_1^a, \omega_2^a, \omega^i]$. The previous 3D VACSy exchange experiment obtained these correlations through a straightforward extension of 2D VACSy by incorporating a hop of the sample rotor during t_m .²⁵ We will refer to this experiment as a 3D switched-angle VACSy (VACSy-S) exchange. According to Fig. 1(b), the magnetization evolves for a fixed time t_1 at a specified rotation axis angle β_1 . During t_m , the rotation axis angle is changed to β_2 , and the signal is acquired during t_2 with a total phase

$$\Phi = \omega^i t_1 + \omega_1^a P_2(\cos \beta_1) t_1 + \omega^i t_2 + \omega_2^a P_2(\cos \beta_2) t_2, \quad (9)$$

which is partitioned along three dimensions, as shown in Table I. The two angles β_1 and β_2 are incremented *independently* in the course of the experiment. These two angles and the signal detection time t_2 make up the three adjustable experimental parameters required for the 3D experiment. To obtain the desired spectral variables, the coordinate axes of the signal acquisition space must be defined as $[P_2(\cos \beta_1)t_1, P_2(\cos \beta_2)t_2, t_2]$ (note that since t_1 is a constant time variable, $\omega^i t_1$ is simply a correctable first order phase shift and is thus ignored). The FIDs acquired with $P_2(\cos \beta_1)=0$ form trajectories on the $\tau_1 = P_2(\cos \beta_1)t_1 = 0$ plane (Fig. 4) with the coordinates $[0, P_2(\cos \beta_2)t_2, t_2]$, which are identical to those of 2D VACSy. The only difference in this experiment is that when $P_2(\cos \beta_1) \neq 0$, the magnetization acquires a phase shift

$$\Delta\Phi = \omega_1^a P_2(\cos \beta_1) t_1 \quad (10)$$

during t_1 evolution. This effectively translates the 2D VACSy planes along the $\tau_1 = P_2(\cos \beta_1)t_1$ axis, filling the 3D

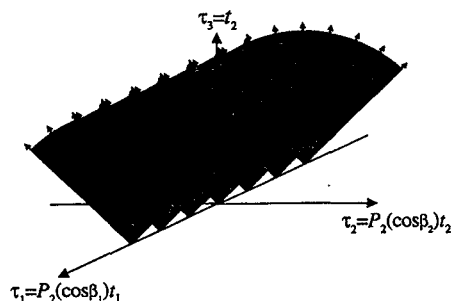


FIG. 4. Trajectories of FIDs for the 3D VACSYS exchange experiment shown in Fig. 1(b). When $P_2(\cos \beta_1)=0$, the signal evolves on the $\tau_1=0$ plane in the identical manner as in the 2D VACSYS experiment shown in Fig. 2. When $P_2(\cos \beta_1) \neq 0$, the signal acquires an additional phase shift, $\Delta\Phi = P_2(\cos \beta_1)t_1\omega_1^a$ that encodes the anisotropic frequencies before the t_m mixing delay. This phase shift results in a translation of the 2D VACSYS plane along the $\tau_1 = P_2(\cos \beta_1)t_1$ dimension, filling the three-dimensional phase space.

phase space, as shown in Fig. 4. The discrete data points acquired at specific angles $\beta_1 = \beta_i$ and $\beta_2 = \beta_j$ are placed in τ space according to the coordinates

$$\tau_1 = P_2(\cos \beta_i)t_1, \quad \tau_2 = RP_2(\cos \beta_j)nt_d, \quad \tau_3 = nt_d, \quad (11)$$

where $R = sw_2^a/sw_1^i$ with sw_2^a being the spectral width in the anisotropic ω_2^a dimension, and sw_1^i being the spectral width in the isotropic ω_1^i dimension. After the data within each τ_1 plane has been interpolated in the same manner as the 2D VACSYS data, the 3D matrix is Fourier transformed to obtain the correlation spectrum.

D. The 3D total VACSYS (VACSYS-T) exchange experiment

In contrast to VACSYS-S, which requires a series of phase modulated 2D VACSYS data sets, the experiment [Fig. 1(c)], introduced in this paper, requires a series of 2D exchange experiments, each recorded at a different rotation axis angle. We refer to this experiment as 3D total VACSYS (VACSYS-T) exchange to draw on the direct analogies to the original 2D VACSYS experiment. Just as 2D VACSYS uses the scaling of one-dimensional powder patterns at each angle to separate the isotropic and anisotropic chemical shifts, 3D VACSYS-T uses the scaling of two-dimensional anisotropic patterns at each angle for the isotropic separation (Fig. 5), and both 2D VACSYS and 3D VACSYS-T require incremental changes in the rotor axis only at the end of the complete pulse sequence.

The three adjustable parameters in this experiment are the angle β , and the two time variables t_1 and t_2 . In addition, the signals for both the $p=+1$ and $p=-1$ coherence pathways in t_1 are acquired (Fig. 6); the $p=-1$ signal forms stimulated echoes during t_2 while the $p=+1$ signal forms antiechoes.²⁷ This separate detection of both coherence pathways is reminiscent of the States acquisition method where cosine and sine amplitude modulated data are acquired separately to obtain a pure-phase 2D spectrum.³⁴ Here, it provides access to larger areas of τ space and reduces truncation artifacts in the line shapes. The phase

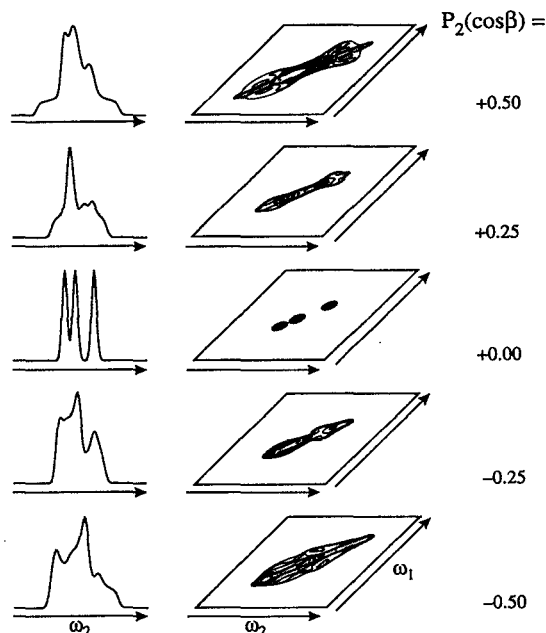


FIG. 5. Scaling of the anisotropic patterns of three different chemical sites at different rotation axis angles β . Simulations of 1D spectra and 2D exchange spectra, corresponding to evolution at different angles β are shown. The anisotropic components of the spectra are scaled by the second Legendre polynomial $P_2(\cos \beta)$, while the isotropic components are left invariant. This scaling of the anisotropic frequency causes the spectral patterns from the three sites to overlap for all but the $P_2=0$ spectra.

$$\Phi = \omega^i p t_1 + \omega_1^a P_2(\cos \beta) p t_1 + \omega^i t_2 + \omega_2^a P_2(\cos \beta) t_2 \quad (12)$$

acquired in each variable-angle spinning 2D exchange experiment is partitioned into three dimensions (Table I), and the τ space coordinate axes are defined as $[P_2(\cos \beta)pt_1, P_2(\cos \beta)t_2, (pt_1 + t_2)]$. Even though these coordinates appear similar in form to those that define τ space for VACSYS-S, because different parameters are being incremented, the FIDs for this experiment form entirely different trajectories.

The placement of the FIDs in τ space can be clarified by considering the geometric patterns generated by different

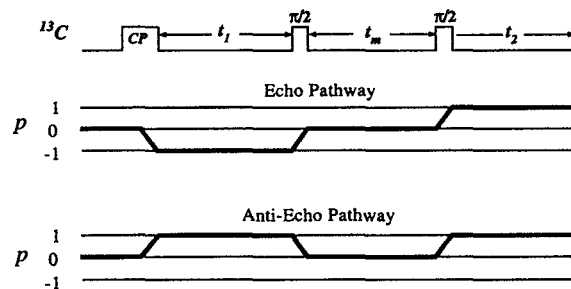


FIG. 6. Coherence pathways for the two sets of data acquired in the 3D VACSYS-T exchange experiment. The echo data are acquired using the $p = -1$ coherence pathway, while the antiecho data are acquired using the $p = +1$ coherence pathway.

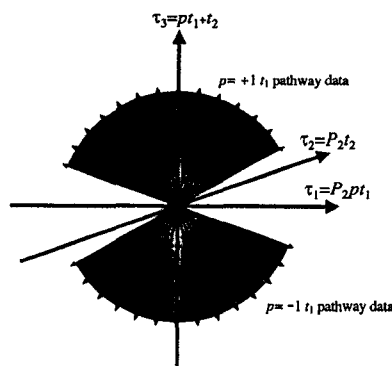


FIG. 7. Mapping of all $t_2=0$ data points in the 3D VACS-T experiment onto the $\tau_2=0$ plane. All the data points map onto the plane with the coordinates $[P_2(\cos \beta)pt_1, 0, pt_1]$. The $p=+1 t_1$ pathway data points are placed on the plane in the same manner as in the 2D VACS-T experiment (Fig. 2). The $p=-1 t_1$ pathway data points are placed below the $\tau_3=0$ plane in an inverted 2D VACS-T pattern.

subsets of the data. The set of data points for $t_2=0$ (the first points of all the FIDs) maps onto the $\tau_2=0$ plane with the phase space coordinates $[P_2(\cos \beta)pt_1, 0, pt_1]$. Aside from the sign factor in p , these coordinates on the $\tau_2=0$ plane are once again identical to those of 2D VACS-T. The $p=+1$ signal forms rays on the plane in the familiar 2D VACS-T pattern, while the $p=-1$ signal forms rays below the $\tau_3=0$ plane in an inverted 2D VACS-T pattern, as illustrated in Fig. 7. For $t_2>0$, the FIDs emerge from the rays on this plane to fill the 3D phase space.

The set of data points for t_1 and t_2 evolution at one specific angle β_i will map onto a skewed plane in the three-dimensional phase space as shown in Fig. 8. These points correspond to the data acquired at the angle β_i during a full 2D exchange experiment. The data points on the $\tau_2=0$ plane form a ray inclined at an angle

$$\alpha_1 = \tan^{-1}[R_1 P_2(\cos \beta_i)] \quad (13)$$

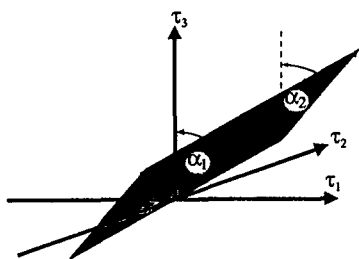


FIG. 8. Trajectories of 3D VACS-T data for t_1 and t_2 evolution at one particular rotation axis angle β_i . The t_1 evolution at β_i for $t_2=0$ is represented by one of the rays from Fig. 7. The ray makes an angle $\alpha_1 = \tan^{-1}[R_1 P_2(\cos \beta_i)]$ with respect to the isotropic τ_3 axis, with half of the ray above the $\tau_3=0$ plane. With t_3 increments, the FIDs emerge from this ray to evolve along the isotropic τ_3 axis as well as the anisotropic τ_2 axis, forming trajectories at an angle $\alpha_2 = \tan^{-1}[R_2 P_2(\cos \beta_i)]$ with respect to the τ_3 axis. Thus the 2D exchange signal acquired at one angle β_i maps onto a skewed plane in the 3D phase space.

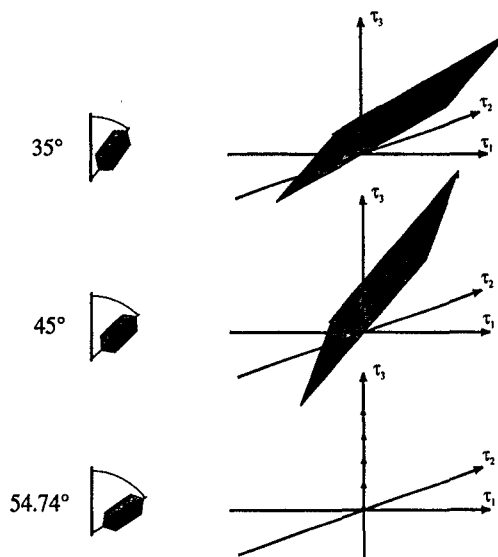


FIG. 9. Trajectories of 3D VACS-T exchange data for t_1 and t_2 evolution at three different rotation axis angles. At different rotation angles β_i , the angles α_1 and α_2 that define the orientation of the data plane in the 3D phase space change, allowing the full 3D phase space to be filled with data. At $\beta_i=54.74^\circ$, $\alpha_1=\alpha_2=0$, and the 2D data plane collapses onto the isotropic axis.

with respect to the isotropic τ_3 axis, where $R_1 = sw_1^a/sw^i$, with sw_1^a being the spectral width in the anisotropic ω_1^a dimension, and sw^i being the spectral width in the isotropic ω^i dimension (Fig. 8). This ray of data corresponds to one of the rays in Fig. 7. With increasing t_2 , evolution not only occurs along the anisotropic τ_2 dimension, but also along the isotropic τ_3 dimension. Thus, unlike conventional 3D NMR experiments, the FIDs do not emerge from the $\tau_2=0$ plane in a perpendicular trajectory, but at an angle

$$\alpha_2 = \tan^{-1}[R_2 P_2(\cos \beta_i)], \quad (14)$$

with respect to the isotropic axis, where $R_2 = sw_2^a/sw^i$, and sw_2^a is the spectral width in the anisotropic ω_2^a dimension (Fig. 8). Figure 9 shows how the data acquired at other rotation axis angles form trajectories in similar 2D planes, but skewed at different angles α_1 and α_2 . Note that when $\beta_i=54.74^\circ$ (the magic angle), the entire plane collapses on to the isotropic axis, since at this angle, $P_2=0$, and no anisotropic evolution occurs. This change in the orientation of the 2D exchange data planes for different β_i allows the 3D τ space to be densely filled with data.

We chose to densely fill only half of the full 3D τ space. Thus all data points that map below the $\tau_3=0$ plane are complex conjugated and spatially inverted into the upper four octants, where the data are interpolated onto a $128 \times 128 \times 128$ Cartesian matrix. The interpolation is simplified when t_1 and t_2 increments are identical. Then $R_1=R_2$ and all of the data points lie on equally spaced planes perpendicular to the isotropic τ_3 axis. In this case, 2D interpolation is required on each of these planes, while no interpolation is required along the isotropic dimension. The patterns made by the experimental data on some of the τ_3 planes are shown in Fig. 10.

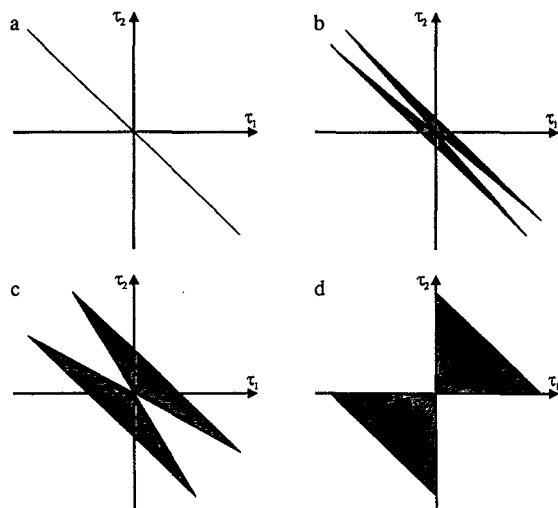


FIG. 10. The patterns made by data points on different isotropic planes perpendicular to the τ_3 axis. For these patterns, all the data have been mapped onto the 3D phase space. Data points originally below the $\tau_3=0$ plane have been complex conjugated and spatially inverted into the upper half of the phase space as described in the text. (a) The $\tau_3=0$ plane. Only a single ray of data exists on this plane along the $\tau_2=-\tau_1$ line. The rest of the area on the plane contains no data, and thus all the points outside of the line are set to zero. The data on this plane correspond to the stimulated-echo tops. (b) and (c) show the data mappings for higher τ_3 planes. As τ_3 increases, the portions of the phase space containing data (the shaded regions) also increase; the regions outside of this area are set to zero. (d) The data mapping onto the highest isotropic plane at $\tau_3=Nt_d$, where $N+1$ is the total number of t_1 or t_2 data points. The data on this plane occupy only two of the quadrants.

Further details of the coordinate calculations and the interpolation procedure are given in the following section. After interpolation, a 3D Fourier transformation yields the final spectrum.

The data rearrangement procedure required for both 3D VACSYS exchange experiments is an extension of the procedure used in 2D VACSYS. All three experiments require tracing out linear trajectories of FIDs in τ space tilted at angles determined by the rotation axis orientations and the relative anisotropic and isotropic spectral widths. In fact, an excellent check of the interpolation routine for 3D VACSYS-T exchange is to examine the $\tau_1=0$ or the $\tau_2=0$ planes in the 3D time domain data matrix after interpolation. Since the coordinates for the data on these planes are identical to those of 2D VACSYS, a Fourier transformation of the time domain data from these planes gives the same spectrum as the 2D VACSYS experiment.

III. COORDINATE MAPPING OF 3D VACSYS-T EXCHANGE

A. General properties of the VACSYS-T coordinates

During t_2 evolution, the $p = -1t_1$ pathway signal forms stimulated echoes, while the $p = +1t_1$ pathway signal forms antiechoes. The data are thus separated into four arrays D_a^+ , D_a^- , D_e^+ , and D_e^- , depending on the sign of the parameters for the different variable-angle experiments. The + and - superscripts designate the sign of P_2 , while a and e sub-

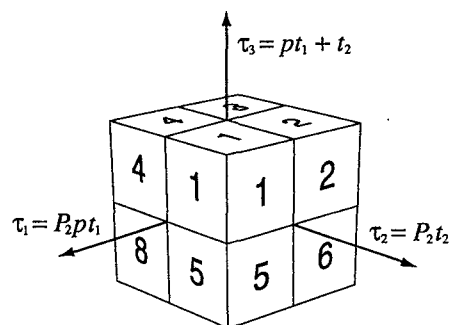


FIG. 11. Labeling of the octants in the 3D phase space. All the octants of the 3D cube are shown and numbered, except octant 7 which is hidden in the perspective shown in the figure.

scripts designate the sign of the t_1 pathway. The array elements are specified by three indices $D(i,j,k)$; i denotes the angle at which the experiment took place, j denotes the t_1 increment, and k denotes the t_2 increment. These indices have the following bounds:

$$1 \leq i \leq N_a, \quad 0 \leq j \leq N_1, \quad 0 \leq k \leq N_2, \quad (15)$$

where N_a is the number of different angles used in the experiment, N_1+1 is the number of t_1 points, and N_2+1 is the number of t_2 points. For notational simplicity, we will assume $N_1=N_2=N$ and $R_1=R_2=1$.

Using the labeling of the octants in Fig. 11, the data contained in each of the four arrays can be shown to map into different regions of the phase space, as listed in Table II. Since the antiecho signal evolves with $\tau_3=t_1+t_2$, the D_a^+ and D_a^- data points map only above the $\tau_3=0$ plane. When $P_2>0$, the antiecho signal evolves along the $+\tau_1$ and $+\tau_2$ axes, which restricts the mapping of the D_a^+ data points to octant 1. Likewise, when $P_2<0$, the antiecho signal evolves along the $-\tau_1$ and $-\tau_2$ axes, restricting the mapping of the D_a^- data points to octant 3. In contrast, the echo signal evolves with $\tau_3=-t_1+t_2$; thus the D_e^+ and D_e^- data points map above and below the $\tau_3=0$ plane. The $\tau_3=0$ plane itself contains all of the stimulated echo tops. When $P_2>0$, the echo signal evolves along the $-\tau_1$ and $+\tau_2$ axes, which restricts the mapping of the D_e^+ data points to octant 6 if $\tau_3<0$ and to octant 2 if $\tau_3>0$. When $P_2<0$, the echo signal evolves along the $+\tau_1$ and $-\tau_2$ axes, which restricts the mapping of the D_e^- data points to octant 8 if $\tau_3<0$ and to octant 4 if $\tau_3>0$. As mentioned above, all of the data points that map below the $\tau_3=0$ plane are complex conjugated and spatially

TABLE II. Regions of the Fourier space mapped by each of the four data arrays. The octants are defined in Fig. 11. The integers i , j , and k index the rotation axis angle, t_1 increments, and t_2 increments, respectively.

p (t_1 path)	P_2 ($\cos \beta$)	Data array	Mapping region
+1	+	$D_a^+(i,j,k)$	Octant 1
+1	-	$D_a^-(i,j,k)$	Octant 3
-1	+	$D_e^+(i,j,k)$	Octants 2, 6
-1	-	$D_e^-(i,j,k)$	Octants 4, 8

TABLE III. Coordinates for the antiecho data points that map directly into octant 1.

$l = j + k$	r	$\tau_1 = P_2 j t_d$	$\tau_2 = P_2 k t_d$	Data points $D_a^+(i, j, k)$
0	1	0	0	$D_a^+(i, 0, 0)$
1	1	$P_2(\cos \beta_i) t_d$	0	$D_a^+(i, 1, 0)$
1	2	0	$P_2(\cos \beta_i) t_d$	$D_a^+(i, 0, 1)$
2	1	$P_2(\cos \beta_i) 2 t_d$	0	$D_a^+(i, 2, 0)$
2	2	$P_2(\cos \beta_i) t_d$	$P_2(\cos \beta_i) t_d$	$D_a^+(i, 1, 1)$
2	3	0	$P_2(\cos \beta_i) 2 t_d$	$D_a^+(i, 0, 2)$
n	$1 \leq r \leq n+1$	$P_2(\cos \beta_i)(n+1-r) t_d$	$P_2(\cos \beta_i)(r-1) t_d$	$D_a^+(i, n+1-r, r-1)$

inverted to the upper four octants. Thus the data points originally mapping into octant 6 will end up in octant 4, while the points originally mapping into octant 8 will end up in octant 2.

The τ space coordinates for 3D VACS-T exchange in Table I may be written in discrete index form by substituting $t_1 = p j t_d$ and $t_2 = k t_d$. With an additional index l defining the isotropic τ_3 increments

$$l = p j + k, \quad (16)$$

and using the condition $R_1 = R_2 = 1$, we obtain

$$\begin{aligned} \tau_1 &= P_2(\cos \beta_i) p j t_d, & \tau_2 &= P_2(\cos \beta_i) (l - p j) t_d, \\ \tau_3 &= l t_d, \end{aligned} \quad (17)$$

where the bounds in l are set to $-N \leq l \leq N$. As described above, all the data points lie on one of the equally spaced isotropic planes indexed by the integer l , and from Eq. (17), the index j locates the data points within each of these planes. The calculation of the τ_1 and τ_2 coordinates, required for interpolation on these planes, will now be discussed. All of the results presented below are summarized in Tables III–V.

B. Mapping of the antiecho data

All of the antiecho data D_a^+ map into octant 1 (Fig. 12) and are acquired with $p = +1$, so Eq. (16) becomes

$$l = j + k. \quad (18)$$

On the $l=0$ plane [Fig. 12(a)], only $j=0$ satisfies Eq. (18) and the bounds in Eq. (15). Thus all of the data points $D_a^+(i, 0, 0)$ map into the same coordinate on the $l=0$ plane

$$\tau_1 = 0, \quad \tau_2 = 0. \quad (19)$$

These points correspond to the data acquired with zero time evolution in both t_1 and t_2 .

On the $l=1$ plane [Fig. 12(b)], Eqs. (15) and (18) are satisfied for $j=0, 1$. Substituting $j=0$ into Eq. (17), the coordinates for $D_a^+(i, 0, 1)$ become

$$\tau_1 = 0, \quad \tau_2 = P_2(\cos \beta_i) t_d. \quad (20)$$

Likewise, substituting $j=1$, the $D_a^+(i, 1, 0)$ coordinates become

$$\tau_1 = P_2(\cos \beta_i) t_d, \quad \tau_2 = 0. \quad (21)$$

These points form two rays, one along each of the axes in the plane, with each ray containing N_a data points.

On the $l=2$ plane [Fig. 12(c)], there are three rays of data corresponding to $j=0, 1$, and 2. The coordinates on this plane are obtained in the same manner as above and are listed in Table III. In general, the $l=n$ plane has $n+1$ rays of data. With the rays indexed by the integer r and numbered counterclockwise from the τ_1 axis (Fig. 12), each ray contains the data points $D_a^+(i, n+1-r, r-1)$ with the coordinates

$$\tau_1 = P_2(\cos \beta_i)(n+1-r) t_d, \quad \tau_2 = P_2(\cos \beta_i)(r-1) t_d. \quad (22)$$

The data points in D_a^- map into τ space in the identical manner as described above except that since $P_2 \leq 0$, the data maps into octant 3 and all the coordinates undergo a sign inversion $(\tau_1, \tau_2) \rightarrow (-\tau_1, -\tau_2)$. Table III summarizes the results of this subsection.

C. Mapping of the echo data

The mapping for the echo data differs from the antiecho mapping in that the echo data points map both above and

TABLE IV. Coordinates for the echo data points with $P_2 \geq 0$ that map directly into octant 2.

$l = -j + k$	r^a	$\tau_1 = -P_2 j t_d$	$\tau_2 = P_2 k t_d$	Data points $D_e^+(i, j, k)$
N	1	0	$P_2(\cos \beta_i) N t_d$	$D_e^+(i, 0, N)$
$N-1$	1	0	$P_2(\cos \beta_i)(N-1) t_d$	$D_e^+(i, 0, N-1)$
$N-1$	2	$-P_2(\cos \beta_i) t_d$	$P_2(\cos \beta_i) N t_d$	$D_e^+(i, 1, N)$
$N-2$	1	0	$P_2(\cos \beta_i)(N-2) t_d$	$D_e^+(i, 0, N-2)$
$N-2$	2	$-P_2(\cos \beta_i) t_d$	$P_2(\cos \beta_i)(N-1) t_d$	$D_e^+(i, 1, N-1)$
$N-2$	3	$-P_2(\cos \beta_i) 2 t_d$	$P_2(\cos \beta_i) N t_d$	$D_e^+(i, 2, N)$
n	$1 \leq r^a \leq N-n+1$	$-P_2(\cos \beta_i)(r^a-1) t_d$	$P_2(\cos \beta_i)(n+r^a-1) t_d$	$D_e^+(i, r^a-1, n+r^a-1)$

TABLE V. Coordinates for the echo data points with $P_2 \leq 0$ that map into octant 2 through complex conjugation and spatial inversion.

$l = -j + k$	r^b	$\tau_1 = - P_2 j t_d$	$\tau_2 = P_2 k t_d$	Data points $D_e^{-*}(i, j, k)$
N	1	$- P_2(\cos \beta_i) N t_d$	0	$D_e^{-*}(i, N, 0)$
$N-1$	1	$- P_2(\cos \beta_i) (N-1) t_d$	0	$D_e^{-*}(i, N-1, 0)$
$N-1$	2	$- P_2(\cos \beta_i) N t_d$	$ P_2(\cos \beta_i) t_d$	$D_e^{-*}(i, N, 1)$
$N-2$	1	$- P_2(\cos \beta_i) (N-2) t_d$	0	$D_e^{-*}(i, N-2, 0)$
$N-2$	2	$- P_2(\cos \beta_i) (N-1) t_d$	$ P_2(\cos \beta_i) t_d$	$D_e^{-*}(i, N-1, 1)$
$N-2$	3	$- P_2(\cos \beta_i) N t_d$	$ P_2(\cos \beta_i) 2 t_d$	$D_e^{-*}(i, N, 2)$
n	$1 \leq r^b \leq N-n+1$	$- P_2(\cos \beta_i) (n+r^b-1) t_d$	$ P_2(\cos \beta_i) (r^b-1) t_d$	$D_e^{-*}(i, n+r^b-1, r^b-1)$

below the $l=0$ plane. The points that originally mapped into the lower half of the phase space are inverted into the upper half before interpolation and Fourier transformation. Thus, two sets of data appear on each plane (Fig. 13); set a corresponds to the data points that map directly onto the plane; set b corresponds to the points that map through spatial inversion. According to Table II, set a of octant 2 contains D_e^{+*} data points, while set b contains D_e^{-*} data points that originally mapped into octant 8, but were complex conjugated and inverted into octant 2. Likewise, set a of octant 4 contains D_e^{-} data points, while set b contains D_e^{+*} . The echo

data mapping also differs in that the plane with the fewest number of data points is the highest isotropic plane [Fig. 13(a)], so we will begin analysis of the echo data coordinates by examining the mapping onto octant 2 with $l=N$ and proceed to lower l planes.

For the echo data, $p = -1$ so Eq. (16) becomes

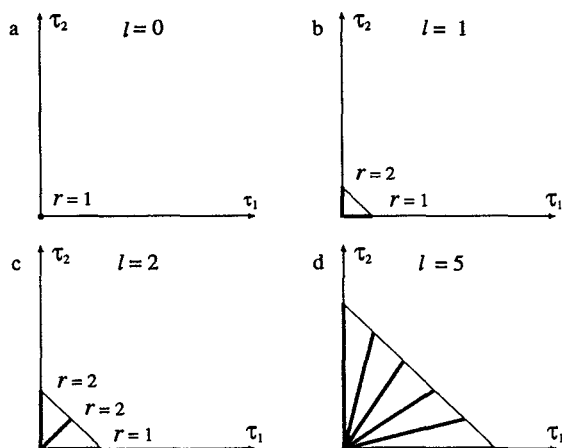


FIG. 12. Mapping of data onto τ_3 planes in octant 1. The planes are shown in *ascending* order starting from the $l=0$ plane. This portion of the phase space is mapped by the antiecho data with $P_2 \geq 0$ contained in the array D_a^{+} . The bold lines represent the rays of experimental data points that are placed in each of the planes. The rays of data are labeled by the index r and are numbered counterclockwise starting from the τ_1 axis. The specific coordinates and data points mapping into this octant are given in Table III and are discussed in the text. (a) The $l=0$ plane. There is only a single point in this plane corresponding to zero evolution in both t_1 and t_2 . (b) The $l=1$ plane. The data map onto two rays, one along each of the two anisotropic axes on the plane. The data correspond to the signal obtained from a single dwell time increment in either t_1 or t_2 . Each of the two rays contains N_d data points. (c) The $l=2$ plane. There are three rays of data on this plane corresponding to three different combinations of t_1 and t_2 dwell time increments to obtain $i+j=2$. (d) The $l=5$ plane. With each higher increment of the τ_3 plane, one additional ray of data appears and the portion of the phase space covered by the data increases. There are six rays of data on this plane. Altogether, plane l contains $l+1$ rays of data, with each ray containing N_d data points.

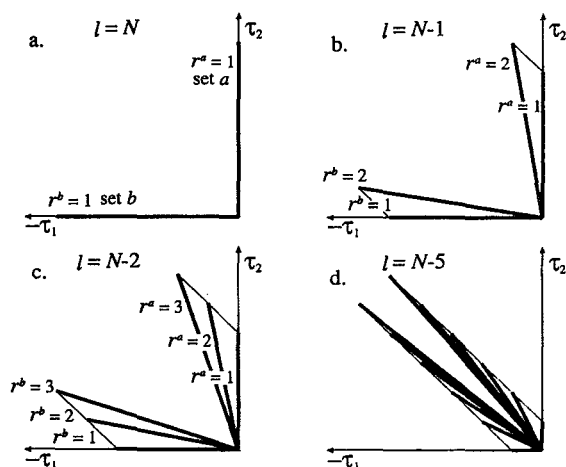


FIG. 13. Mapping of the echo data D_e^{-*} and D_e^{+*} onto octant 2. The planes are shown in *descending* order from the highest isotropic plane at $l=N$. The data in this octant are separated into two sets. Set a contains the data D_e^{+*} that map directly onto the octant. Set b contains the data D_e^{-*} that map into octant 2 through complex conjugation and spatial inversion of D_e^{-} that originally mapped into octant 8. The rays of data in set a are indexed by r^a and are numbered counterclockwise starting from the $+\tau_2$ axis; the rays in set b are indexed by r^b and are numbered clockwise starting from the $-\tau_1$ axis. The data points that map onto this octant and their coordinates are given in Tables IV and V and are discussed in the text. (a) The $l=N$ plane. Two rays of data appear on this plane. The D_e^{+*} data that have evolved with $j=0$ and $k=N$ map onto the τ_2 axis. The D_e^{-*} data that have evolved with $j=N$ and $k=0$ map onto the $-\tau_1$ axis. (b) The $l=N-1$ plane. Two rays appear on this plane for each set of data. The two rays in set a correspond to the two possible combinations of t_1 and t_2 dwell times that satisfy the condition $-j+k=N-1$. The two rays in set b require the dwell time combinations to satisfy $-j+k=-(N-1)$. (c) The $l=N-2$ plane. There are three rays for each set of data. The three rays in set a correspond to the three possible combinations of t_1 and t_2 dwell times that satisfy $-j+k=N-2$. The three rays in set b require the dwell time combinations to satisfy $-j+k=-(N-2)$. (d) The $l=N-5$ plane. With each decrement of τ_3 , an additional ray appears for each set of data. However, the area of phase space the data cover becomes smaller at the lower planes until at $\tau=0$ all the rays collapse onto a single line at $\tau_2 = -\tau_1$.

$$l = -j + k. \quad (23)$$

On the $l=N$ plane [Fig. 13(a)], D_e^+ data points in set a satisfy Eqs. (15) and (23) only if $j=0$. Substituting $j=0$ into Eq. (17), the coordinates for $D_e^+(i,0,N)$ on the plane become

$$\tau_1 = 0, \quad \tau_2 = P_2(\cos \beta_i) N t_d. \quad (24)$$

The data points in set b originally mapped into the $l=-N$ plane of octant 8, requiring $j=N$ and the coordinates

$$\tau_1 = |P_2(\cos \beta_i)| N t_d, \quad \tau_2 = 0. \quad (25)$$

With complex conjugation and spatial inversion of coordinates $(\tau_1, \tau_2, \tau_3) \rightarrow (-\tau_1, -\tau_2, -\tau_3)$, the $D_e^{-*}(i,N,0)$ points map onto the $l=N$ plane with the final coordinates

$$\tau_1 = -|P_2(\cos \beta_i)| N t_d, \quad \tau_2 = 0. \quad (26)$$

The data in set a can be seen in Fig. 13(a) to form a ray along the τ_2 axis, while the data in set b forms a ray along the $-\tau_1$ axis.

On the $l=N-1$ plane [Fig. 13(b)], set a contains two rays of data corresponding to $j=0,1$. For $j=0$, $D_e^+(i,0,N-1)$ maps onto this plane with the coordinates

$$\tau_1 = 0, \quad \tau_2 = P_2(\cos \beta_i)(N-1)t_d, \quad (27)$$

while for $j=1$, $D_e^+(i,1,N)$ has the coordinates

$$\tau_1 = -P_2(\cos \beta_i)t_d, \quad \tau_2 = P_2(\cos \beta_i)Nt_d. \quad (28)$$

Likewise, set b on this plane also contains two rays of data, corresponding to the points that originally mapped into the $l=-(N-1)$ plane with $j=N-1, N$. After the final transformation, $D_e^{-*}(i,N-1,0)$ maps onto the $l=N-1$ plane with the coordinates

$$\tau_1 = -|P_2(\cos \beta_i)|(N-1)t_d, \quad \tau_2 = 0, \quad (29)$$

while $D_e^{-*}(i,N,1)$ has the coordinates

$$\tau_1 = -|P_2(\cos \beta_i)| N t_d, \quad \tau_2 = |P_2(\cos \beta_i)| t_d. \quad (30)$$

On the $l=N-2$ plane [Fig. 13(c)], set a contains three rays of data corresponding to $j=0,1,2$, and set b also contains three rays of data corresponding to $j=N-2, N-1, N$. The data points and coordinates on this plane are given in Tables IV and V. In general, the $l=n$ plane has a total of $N-n+1$ rays of data for each of the two sets a and b . Figure 13 shows the rays of data in set a indexed by r^a and numbered counterclockwise from the $+\tau_2$ axis; rays in set b are indexed by r^b and numbered clockwise from the $-\tau_1$ axis. On the $l=n$ plane, each ray in set a contains the data points $D_e^+(i, r^a-1, n+r^a-1)$ with the coordinates

$$\begin{aligned} \tau_1 &= -|P_2(\cos \beta_i)|(r^a-1)t_d, \\ \tau_2 &= |P_2(\cos \beta_i)|(n+r^a-1)t_d, \end{aligned} \quad (31)$$

while each ray in set b contains $D_e^{-*}(i, n+r^b-1, r^b-1)$ with the coordinates

$$\begin{aligned} \tau_1 &= -|P_2(\cos \beta_i)|(n+r^b-1)t_d, \\ \tau_2 &= |P_2(\cos \beta_i)|(r^b-1)t_d. \end{aligned} \quad (32)$$

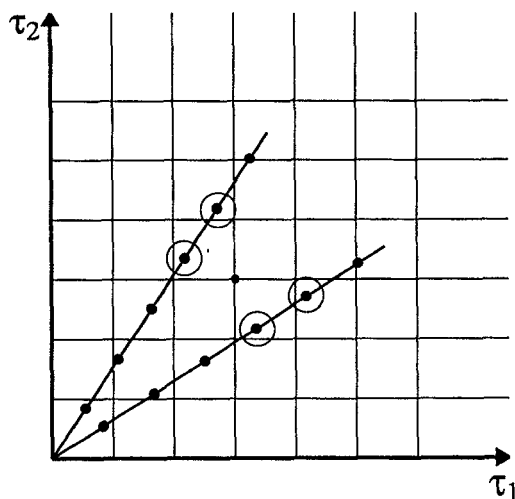


FIG. 14. Interpolation of the data points onto a Cartesian grid. All the data points lie on one of the τ_3 planes, requiring a 2D interpolation on each of the planes. Only the points within the shaded regions of Fig. 10 are interpolated. In this region, each point on the Cartesian grid is bounded by two rays of experimental data. Four nearest neighbor points (circled in the figure) are chosen from the two rays to interpolate the Cartesian grid point p as discussed in the text.

The mapping into octant 4 is identical to that of octant 2, except that the arrays are swapped $D_e^{-*} \rightarrow D_e^{+*}$ and $D_e^+ \rightarrow D_e^-$, and the coordinates undergo a sign change $(\tau_1, \tau_2) \rightarrow (-\tau_1, -\tau_2)$. Tables IV and V summarize the results of this subsection.

D. Interpolation

Once the coordinates are calculated, the experimental data on each isotropic plane must be interpolated onto a Cartesian grid. Only the points within the shaded bounds of Fig. 10 are interpolated. Any Cartesian grid point p within this region is bounded by two rays of data, and thus four nearest neighbor experimental data points can be obtained, two on each ray (Fig. 14). Any combination of three of these data points forms a plane in the 3D spaces defined by the coordinates $(\text{Re } D, \tau_1, \tau_2)$ and $(\text{Im } D, \tau_1, \tau_2)$, where $\text{Re } D$ and $\text{Im } D$ are the real and imaginary parts of the complex data points. By successively ignoring one of the extra points of the original four, real and imaginary planes may be constructed in four ways. The interpolated value at point p is assigned the average complex value of the intersecting real and imaginary planes at the coordinates of point p .

IV. EXPERIMENT

The 3D VACS-T exchange spectrum was recorded on a 7.07 T, homebuilt spectrometer, interfaced to a TECMAG pulse programmer. Modifications were made to the basic variable angle probe design³⁵ to allow for variable temperature control. The air for both the spinner drive and bearing was temperature controlled separately by heaters placed at the base of the probe, then transferred through Dewared lines into the probe head. The temperature was monitored by an Omega programmable temperature controller and a thermo-

couple placed on the bearing line just before entry into the spinner assembly. The angle of the spinner axis was adjusted by a Whedco stepping motor and a computerized motor controller that allowed angles to be set to within 0.1° . A field gradient in the probe contributed a constant angle dependent frequency shift in the spectra that was removed in the final data processing.

A sample of ordered isotactic polypropylene (iPP) (Hoshtalen PP) $\{[-CH_2CH-(CH_3)-]_n\}$ was obtained from Hoechst AG (Frankfurt, Germany). The sample was cut into disks and placed inside the spinner with the draw axis perpendicular to the axis of rotation.

Each variable angle spinning exchange experiment was obtained at 360 K with a mixing time of 1 s and a recycle delay of 1 s. A conventional ^{13}C cross-polarization sequence was used with 1H decoupling during the t_1 and t_2 time periods.³⁶ Phase cycling³⁷ was used to select the $-1 \rightarrow 0 \rightarrow +1$ and $+1 \rightarrow 0 \rightarrow +1$ pathways, and the data sets were recorded separately. Since the rf coil axis remains parallel to the sample spinner axis, the rotation axis angle β was restricted to the range $90^\circ \geq \beta \geq 35.3^\circ$. Altogether 31 different 2D exchange experiments were recorded at angles corresponding to the P_2 values of

$$P_2(\cos \beta_k) = -0.5 + (k-1)/30, \quad k=1, \dots, 31. \quad (33)$$

Both t_1 and t_2 dwell time increments were set to 166.7 μs . One hundred and twenty-eight points were acquired in t_2 , while the number of points acquired in t_1 varied with the angle at which the 2D exchange experiment took place. For the experiments recorded in the range $59^\circ \geq \beta \geq 52^\circ$, 128 t_1 points were acquired, while for the experiments in the ranges $51^\circ \geq \beta \geq 35.3^\circ$ and $90^\circ \geq \beta \geq 60^\circ$, 64 t_1 points were acquired, since the FIDs decay faster at these latter angles. Only one FID is required at the magic angle $\beta = 54.74^\circ$, where all the anisotropic terms disappear. Each FID was signal averaged for 40 scans and the total data acquisition time for the 3D experiment was four days. The data were then transferred to a Silicon Graphics R4000 computer, where each 2D experiment was zero filled to a 128×128 matrix, phase corrected, and then mapped and interpolated onto a $128 \times 128 \times 128$ cube. The data was then Fourier transformed to obtain the 3D exchange spectrum.

V. RESULTS AND DISCUSSION

Isotactic polypropylene (iPP) is used to demonstrate the 3D VACSYS exchange experiments. X-ray diffraction and NMR studies have revealed that iPP is a semicrystalline polymer forming a helix with three monomers per helix turn (3_1 helix) in the crystalline region.^{38,39} A side view of the helix is shown in Fig. 15(a) and the view along the helix axis with the methyl groups pointing outward is shown in Fig. 15(b). Mechanical and dielectric measurements on iPP have shown that slow motion in the range of 1 Hz to 1 kHz occurs at elevated temperatures.⁴⁰ ^{13}C and 2H NMR studies have shown that iPP undergoes discrete threefold 120° jumps about the helix axis^{22,41} [Fig. 15(b)]. The correlation times strongly indicate that this helical motion is responsible for the α relaxation process. In agreement with these results, the

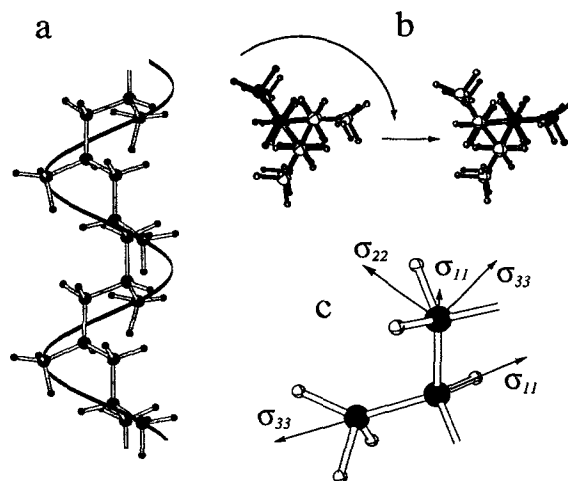


FIG. 15. (a) A side view of the iPP 3_1 helix. (b) A view of the molecule along the helix axis. The threefold helical jump motion is illustrated by the highlighted $(-CH-CH_3)$ group that undergoes a 120° rotation. (c) Orientation of the CSA tensors in the molecular frame. The tensors for the methine and methyl carbons are almost axially symmetric so the unique axis alone describes the orientations of these tensors. The σ_{11} axis of the methine carbon is placed along the C-H bond, and the σ_{33} axis of the methyl carbon is placed along the CH- CH_3 bond. σ_{33} of the methylene carbon is perpendicular to H-C-H plane, while the σ_{22} axis is offset from bisecting the H-C-H angle.

spectra from the previous 3D VACSYS exchange experiment revealed off-diagonal exchange intensity for each of the chemical sites of iPP.²⁵

Ordered iPP is used in this current study to enhance the appearance of the off-diagonal exchange patterns. The ordering of the sample is reflected in distinct anisotropic line shapes that are modified from powder patterns.⁴² Two-dimensional VACSYS experiments reveal these differences in the anisotropic spectra of each chemical site for the disordered and ordered samples as shown in Figs. 16(a) and 16(b). For simulation purposes, the principal values of the chemical shift anisotropy (CSA) tensors were obtained from the powder patterns, and the orientation of each tensor was obtained from literature.⁴³ Figure 15(c) shows the orientation of the CSA tensors for the three chemically distinct carbon sites. The CSA tensors for the methyl and methine carbons are almost axially symmetric, thus the unique axis alone defines the orientation of each tensor in the molecular frame. The σ_{33} axis of the methyl carbon is placed along the C- CH_3 bond, while the σ_{11} axis of the methine carbon is placed along the C-H bond. For the methylene carbon, the σ_{33} axis is perpendicular to the H-C-H plane, and the σ_{22} axis is offset from bisecting the H-C-H angle as specified by Nakai *et al.*⁴³

The well-defined helical structure of the chains leads to a microscopic axial symmetry in the orientation distribution, while the large diameter of the drawn samples leads to a macroscopic axial symmetry. Thus the orientation distribution is constant in two of the three Euler angles (transverse isotropy).⁴⁴ A spherical Gaussian function

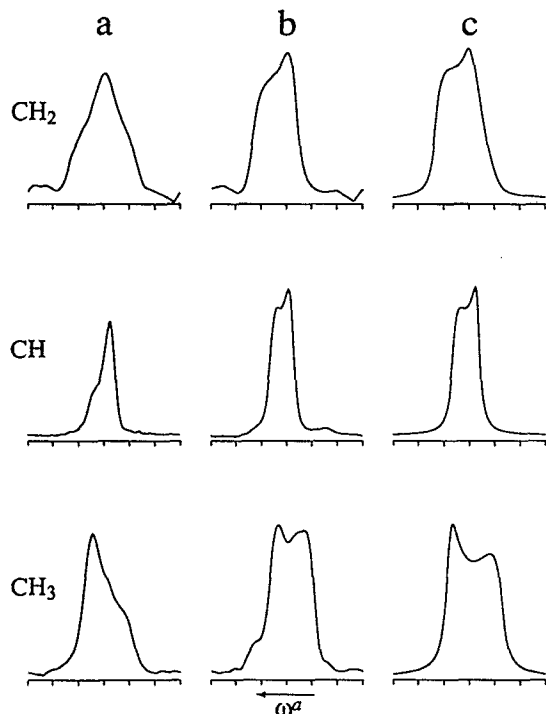


FIG. 16. Experimental 1D ^{13}C anisotropic spectral patterns for the three sites of iPP obtained from 2D VACSYS experiments. The spacing of tick marks corresponds to 1 kHz. (a) Anisotropic spectral line shapes of disordered iPP. (b) Anisotropic spectral line shapes of ordered iPP. (c) Simulations of ordered iPP using a spherical Gaussian orientation distribution function with a rms deviation of 15° .

$$P(\theta) = C \exp\left(\frac{-\sin^2 \theta}{2\theta_\sigma^2}\right) \quad (34)$$

is used as the orientation distribution of the helix axes about the draw axis of the oriented sample.⁴⁵ Here, C is a normalization constant, θ specifies the orientation of a given helix axis with respect to the sample draw axis, and θ_σ is the root mean square of the angular deviation from the order axis. Fits to the experimental data were obtained using $\theta_\sigma = 15^\circ$ and are shown in Fig. 16(c).

The effect of molecular reorientation on the 2D exchange patterns for each carbon site of iPP is clearly seen in Figs. 17(a) and 17(b), which were obtained using mixing times of 1 ms and 1 s, respectively. Since no significant molecular reorientation has occurred during the short mixing delay, the spectra in Fig. 17(a) show only diagonal ridges. Note that such short mixing delays are not technically achievable in the VALSYS exchange experiment due to the duration of the rotor flips during the mixing time. The spectra in Fig. 17(b) reveal distinct off-diagonal ridge patterns, reflecting the molecular reorientation which occurred during the long mixing delay. Simulations shown in Fig. 17(c) using 120° helical jumps with $\tau_c < t_m$, show good agreement with the experimental data. In particular, both the experimental and simulated spectra for the methylene and methine carbons reveal the elliptical ridge patterns indicative of discrete molecular motion.⁴⁶ The exchange pattern for the methyl carbon shows significant discrepancy between experiment and simu-

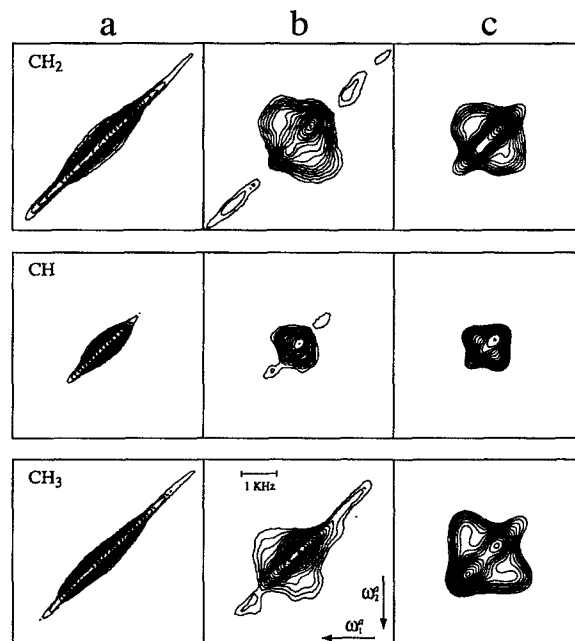


FIG. 17. Experimental 2D exchange patterns for the three sites of ordered iPP obtained from the 3D VACSYS-T exchange experiment at $T = 360$ K. (a) Three-dimensional VACSYS-T exchange data with $t_m = 1$ ms. (b) Three-dimensional VACSYS-T exchange data with $t_m = 1$ s. (c) Simulations of 2D exchange patterns for each site of iPP, using 120° jumps about the helix with a correlation time $\tau_c < t_m$.

lation. However, the methyl line shape distortion is also seen in the 2D VACSYS patterns (not shown) obtained by Fourier transforming either the $\tau_1 = 0$ or the $\tau_2 = 0$ slice from the full 3D VACSYS-T time domain matrix as discussed above. Thus we surmise that the distortion in the methyl carbon exchange pattern is not due to the procedure of the experiment, but rather due to a strong spectral component from the amorphous regions of the polymer at higher temperatures.⁴¹

Artifacts that appear as ridges along the diagonal in the exchange patterns, however, are inherent to the experiment and arise from incomplete sampling of the Fourier space, as seen in Fig. 10. Filling these holes would require refocusing only the anisotropic frequencies during t_2 evolution and would involve a hop of the rotor in between the t_1 and t_2 evolution periods, nullifying the main advantage of the 3D VACSYS-T exchange experiment. Artifacts due to incomplete sampling of Fourier space are also seen in 2D VACSYS,¹⁰ but these artifacts can be removed by using a linear prediction⁴⁷ to fill in the missing data.⁴⁸ We are currently exploring other processing methods that may be suitable for improving the quality of the 3D VACSYS-T exchange spectrum. However, despite the artifacts, distinct patterns revealing discrete jump motions can be clearly seen in the exchange spectrum for two of the three chemical sites in iPP in good agreement with simulations. The quality of the spectra is such that, in the case of an unknown motional mechanism, the spectral patterns can be used, in conjunction with simulations, to reject incorrect motional models and verify the correct mechanisms.

VI. CONCLUSIONS AND OUTLOOK

We have demonstrated a new extension of the VACSY technique for high resolution studies of slow molecular motion which eliminates the need for rapid reorientation of the sample rotor. This new technique is based on the same basic principle as the original 2D VACSY and 3D VACSY-S exchange experiments. The change in the rotation axis of a rapidly spinning sample with respect to the static magnetic field B_0 scales the anisotropic frequencies, but leaves the isotropic frequencies invariant. By acquiring a series of 2D exchange experiments at different rotation axes, the time domain data may be mapped onto a 3D matrix such that a fast Fourier transformation directly yields isotropic–anisotropic correlations. There are two main features particular to 3D VACSY-T exchange. By removing the requirement for the rotor hop, experimental difficulties have been shifted from the hardware and mechanical aspects of the experiment to the software and data processing, which is generally preferable given continued advances in software and computer technology. The experiment also removes restrictions on the length of the t_m mixing delay and opens up the possibility for studying the full range of dynamical rates in the slow motion regime. This study also further demonstrates how a redefinition of the generalized time variables, τ_i , in terms of adjustable experimental parameters can lead to novel experimental approaches.

ACKNOWLEDGMENTS

This work was supported by the Director, Office of Energy Research, Office of Basic Energy Sciences, Material Sciences Division, and Office of Health and Environmental Research, Health Effects Research Division, of the U.S. Department of Energy under Contract No. DE-AC03-76SF000098. L.E. was a fellow of the Miller Institute for Basic Research in Science. K. S.-R. thanks the BASF AG and the German National Scholarship Foundation for a fellowship.

¹ G. M. Clore and A. M. Gronenborn, *Prog. NMR Spectrosc.* **23**, 43 (1991).

² U. Haeberlen, *High Resolution NMR in Solids: Selective Averaging, Advances in Magnetic Resonance* (Academic, New York, 1976), Suppl. 1.

³ E. W. Wooten, K. T. Mueller, and A. Pines, *Acc. Chem. Res.* **25**, 209 (1992).

⁴ E. Lipmaa, M. Alla, and T. Turherm, *Proceedings of the 19th Congress Ampere* (Springer-Verlag, Heidelberg, 1976), p. 241.

⁵ Y. Yarim-Agaev, P. N. Tutunjian, and J. S. Waugh, *J. Magn. Reson.* **47**, 51 (1982).

⁶ T. Nakai, J. Ashida, and T. Terao, *J. Chem. Phys.* **88**, 6049 (1988).

⁷ A. Bax, N. M. Szeverenyi, and G. E. Maciel, *J. Magn. Reson.* **52**, 147 (1983).

⁸ R. Tycko, G. Dabbagh, and P. A. Mirau, *J. Magn. Reson.* **85**, 265 (1989).

⁹ L. Frydman, G. C. Chingas, Y. K. Lee, P. J. Grandinetti, M. A. Eastman, G. A. Barrall, and A. Pines, *J. Chem. Phys.* **97**, 4800 (1992). Equations (10a) and (10b) in this paper should read $\tan(\varphi_{\max}) = DW_i \cdot P_2 \max / DW_a$ and $\tan(\varphi_{\min}) = DW_i \cdot P_2 \min / DW_a$, respectively.

¹⁰ Z. Gan, *J. Am. Chem. Soc.* **114**, 8307 (1992).

¹¹ I. M. Ward, *Mechanical Properties of Solid Polymers* (Wiley, New York, 1971).

¹² R. T. Bailey, A. M. North, and R. A. Pethridge, *Molecular Motions in High Polymers* (Clarendon, Oxford, 1981).

¹³ M. T. Hansen, *Colloid Polymer Sci.* **271**, 446 (1993).

¹⁴ H. W. Spiess, *Dynamic NMR Spectroscopy in Solids* (Springer, Berlin, 1978).

¹⁵ S. Wefing and H. W. Spiess, *J. Chem. Phys.* **89**, 1219 (1988).

¹⁶ C. Schmidt, S. Wefing, B. Blumich, and H. W. Spiess, *Chem. Phys. Lett.* **130**, 84 (1986).

¹⁷ R. R. Vold and R. L. Vold, *Adv. Magn. Opt. Reson.* **16**, 85 (1991).

¹⁸ D. Schaefer and H. W. Spiess, *J. Chem. Phys.* **97**, 7944 (1992).

¹⁹ D. E. Wemmer, D. J. Ruben, and A. Pines, *J. Am. Chem. Soc.* **103**, 28 (1981).

²⁰ M. S. Solum, K. W. Zilm, J. Michl, and D. M. Grant, *J. Phys. Chem.* **87**, 2940 (1983).

²¹ A. Hagemeyer, K. Schmidt-Rohr, and H. W. Spiess, *Adv. Magn. Reson.* **13**, 85 (1989).

²² L. Frydman, G. C. Chingas, Y. K. Lee, P. J. Grandinetti, M. A. Eastman, G. A. Barrall, and A. Pines, *Isr. J. Chem.* **32**, 161 (1992).

²³ J. W. Zwanziger, K. K. Olsen, and S. L. Tagg, *Phys. Rev. B* **47**, 14618 (1993).

²⁴ L. Frydman, S. Vallabhaneni, Y. K. Lee, and L. Emsley, *J. Chem. Phys.* (in press).

²⁵ L. Frydman, Y. K. Lee, L. Emsley, G. C. Chingas, and A. Pines, *J. Am. Chem. Soc.* **115**, 4825 (1993).

²⁶ C. Griesinger, O. W. Sørensen, and R. R. Ernst, *J. Magn. Reson.* **84**, 14 (1989).

²⁷ R. R. Ernst, G. Bodenhausen, and A. Wokaun, *Principles of Nuclear Magnetic Resonance in One and Two Dimensions* (Clarendon, Oxford, 1987).

²⁸ W. A. Edelstein, J. M. Hutchison, G. Johnson, and T. W. Redpath, *Phys. Med. Biol.* **25**, 751 (1980).

²⁹ D. B. Twieg, J. Katz, and R. M. Peshock, *Magn. Reson. Med.* **5**, 32 (1987).

³⁰ D. G. Cory, J. B. Miller, A. N. Garroway, and W. S. Veeman, *J. Magn. Reson.* **85**, 219 (1989).

³¹ L. Frydman, J. S. Harwood, D. N. Garnier, and G. C. Chingas, *J. Magn. Reson. A* **101**, 240 (1993).

³² C. B. Ahn, J. H. Kim, and Z. H. Cho, *IEEE Trans. Med. Imaging* **5**, 2 (1986).

³³ G. C. Chingas, L. Frydman, G. A. Barrall, and J. S. Harwood, *Magnetic Resonance Microscopy Methods and Applications in Materials Science, Agriculture and Biomedicine* (VCH, Weinheim, Germany, 1992).

³⁴ D. J. States, R. A. Haberkorn, and D. J. Ruben, *J. Magn. Reson.* **48**, 286 (1982).

³⁵ M. A. Eastman, P. J. Grandinetti, Y. K. Lee, and A. Pines, *J. Magn. Reson.* **98**, 333 (1992).

³⁶ A. Pines, M. G. Gibby, and J. S. Waugh, *J. Chem. Phys.* **59**, 569 (1973).

³⁷ G. Bodenhausen, H. Kogler, and R. R. Ernst, *J. Magn. Reson.* **58**, 370 (1984).

³⁸ Z. Mencik, *J. Macromol. Sci. Phys. B* **6**, 101 (1972).

³⁹ A. Bunn, M. E. A. Cudby, R. K. Harris, K. J. Packer, and B. J. Say, *Polymer* **23**, 694 (1982).

⁴⁰ N. G. McCrum, B. E. Read, and G. Williams, *Anelastic and Dielectric Effects in Polymeric Solids* (Wiley, New York, 1967).

⁴¹ D. Schaefer, H. W. Spiess, U. W. Suter, and W. W. Fleming, *Macromolecules* **23**, 3431 (1990).

⁴² R. Hentschel, J. Schlitter, H. Sillescu, and H. W. Spiess, *J. Chem. Phys.* **68**, 56 (1978).

⁴³ T. Nakai, J. Ashida, and T. Terao, *Magn. Res. Chem.* **27**, 666 (1989).

⁴⁴ G. S. Harbison, V. Vogt, and H. W. Spiess, *J. Chem. Phys.* **86**, 1206 (1987).

⁴⁵ B. F. Chmelka, K. Schmidt-Rohr, and H. W. Spiess, *Macromolecules* **26**, 2282 (1993).

⁴⁶ S. Wefing, S. Kaufmann, and H. W. Spiess, *J. Chem. Phys.* **89**, 1234 (1988).

⁴⁷ S. M. Kay, *Modern Spectral Estimation Theory and Application* (Prentice-Hall, Englewood Cliffs, NJ, 1988).

⁴⁸ Y. K. Lee, Y. Y. Lin, A. Pines, R. L. Vold, and G. L. Hoatson, *J. Magn. Reson.* (submitted).